

Development of intergranular thermal residual stresses in beryllium during cooling from processing temperatures

D.W. Brown^{*}, T.A. Sisneros, B. Clausen, S. Abeln, M.A.M. Bourke,
B.G. Smith, M.L. Steinzig, C.N. Tomé, S.C. Vogel

Los Alamos National Laboratory, Los Alamos, NM 87545, USA

Received 2 May 2008; received in revised form 11 September 2008; accepted 15 September 2008

Available online 12 January 2009

Abstract

The intergranular thermal residual stresses in texture-free solid polycrystalline beryllium were determined by comparison of crystallographic lattice parameters in solid and powder samples measured by neutron diffraction during cooling from 800 °C. The internal stresses are not significantly different from zero >575 °C and increase nearly linearly <525 °C. At room temperature, the *c* axis of an average grain is under ~200 MPa of compressive internal stress, and the *a* axis is under 100 MPa of tensile stress. For comparison, the stresses have also been calculated using an Eshelby-type polycrystalline model. The measurements and calculations agree very well when temperature dependence of elastic constants is accounted for, and no plastic relaxation is allowed in the model.

© 2008 Acta Materialia Inc. Published by Elsevier Ltd. All rights reserved.

Keywords: Neutron diffraction; Residual stresses; Beryllium; Powder processing

1. Introduction

Beryllium and other hexagonal close packed (hcp) metals such as magnesium and zirconium have been the subject of much increased study in recent years. This is in part because of their properties, such as high strength-to-weight ratio and corrosion resistance, which are of interest in the fields of aerospace engineering, transport and energy production. But, also because the relatively low symmetry crystal structure represents the next logical extension of polycrystalline plasticity models which were originally developed for simpler cubic materials. The inherent anisotropy of the hcp metals and the activation of multiple deformation modes, both slip and twinning, greatly increases the complexity of the model, the need for a fundamental understanding, and the need for a more sophisticated experimental characterization.

Materials with low symmetry structures, such as hcp and orthorhombic, in general possess anisotropic coefficients

of thermal expansion (CTE) in the principal crystal coordinate system. Thus, on cooling from any processing step, intergranular thermal residual (ITR) stresses are bound to develop as a result of orientation-dependent contraction in neighboring grains. The most obvious example of these ITR stresses (and strains) is the macroscopic plastic deformation of orthogonal α -uranium during repeated thermal cycling [1]. While less dramatic, they often play an important role in the micro-mechanics of deformation of hexagonal materials as well. Piercy [2] first calculated an upper bound of the ITR stresses in zircaloy ($\alpha_a = 5.7 \times 10^{-6} \text{ }^\circ\text{C}^{-1}$, $\alpha_c = 11.4 \times 10^{-6} \text{ }^\circ\text{C}^{-1}$ [3]) by placing an included grain with anisotropic CTE in an infinitely stiff medium with an isotropic average CTE representing the surrounding polycrystal. In 1989, MacEwen et al. [3] measured ITR stresses in swaged zircaloy bar by comparing the crystallographic CTE measured by neutron diffraction in the polycrystalline bar with that in a single crystal and related them to the observed tension–compression asymmetry in the alloy. In 1996, Tomé et al. [4] determined the ITR stresses in zircaloy through a combined neutron diffraction and elastic–plastic self-consistent (EPSC)

^{*} Corresponding author. Tel.: +1 505 661 2385.

E-mail address: dbrown@lanl.gov (D.W. Brown).

model. Later, Pang et al. [5] measured the ITR stresses in zircaloy 2 through careful absolute measurements of the lattice parameters along select sample orientations, and again compared the results with EPSC calculations.

While the thermal expansion anisotropy in beryllium ($\alpha_a = 12.42 \times 10^{-6} \text{ } ^\circ\text{C}^{-1}$, $\alpha_c = 9.881 \times 10^{-6} \text{ } ^\circ\text{C}^{-1}$ [6]) is considerably smaller than that in zirconium, it is still significant. Moreover, hot-pressed beryllium is nearly texture free, in contrast to a wrought zirconium alloy with strong textures (most grains have similar orientations). The random texture intensifies the grain-to-grain interaction stresses caused by the anisotropic thermal expansion. Similarly to MacEwan et al. [3] for zircaloy, Brown et al. [7] attributed the tension–compression asymmetry of randomly textured beryllium to the ITR stresses.

This work reports the development of ITR stresses in hot-pressed beryllium with nearly random texture as a function of temperature. The ITR stresses are not significantly different from zero above $\sim 575 \text{ } ^\circ\text{C}$, indicating that the material lacks the strength to maintain grain-scale stresses. Below $\sim 525 \text{ } ^\circ\text{C}$, the ITR stresses develop in a manner consistent with the predictions of EPSC model calculations. This cross-over temperature represents the point at which the strength of the beryllium becomes sufficient to allow the buildup of intergranular stresses, and is an important parameter for future EPSC and other model calculations. At room temperature, ITR stresses of $\sim -200 \text{ MPa}$ (compression) are observed along the c axis and 100 MPa (tension) along the prism directions ($\sim 2/3$ and $\sim 1/3$ of the UTS, respectively).

2. Experimental

2.1. Sample preparation

Beryllium has properties that are relatively unique, allowing for direct accurate measurements of the ITR stresses. Because the difference in thermal expansion between the powder and solid is very small compared with the overall thermal expansion ($\sim 400 \text{ } \mu\text{m}$ compared with $12,000 \text{ } \mu\text{m}$ on cooling from $800 \text{ } ^\circ\text{C}$ to room temperature), it was necessary to keep the microstructure of the solid and powder samples as similar and invariant as possible throughout the thermal cycles. For instance, it is important that grain growth does not occur in beryllium until temperatures much higher than those studied here are reached.

A fine powder was used so that only a few crystallites comprised each particulate, ensuring the powder was stress free on the grain scale. The powder was impact ground and air classified to a particle size $< 44 \text{ } \mu\text{m}$. A low impurity powder source, SP65 (0.7% BeO, 0.05% Fe, 0.03% Si, 0.02% C, 0.02% Al, $> 0.01\%$ Mg, and balance Be), was used so that minimal chemical changes would occur during the compaction of the solid. Moreover, the impurities that are present are relatively insoluble in beryllium and are generally immobile and located on the surface of the particulates and on the grain boundaries after compaction.

The beryllium powder was loaded into a cylindrical niobium can (5 mm ID, 10 mm OD, 20 mm tall) with no packing, to reduce contact stresses as much as possible. A niobium lid was electron beam welded into the can in an evacuated chamber. After the neutron diffraction experiments (i.e., heating to $800 \text{ } ^\circ\text{C}$ and returning to room temperature), a small hole was drilled in the niobium can and epoxy infiltrated under pressure to encase the powder for metallurgical investigation.

The solid sample was hot pressed in a steel can at $1000 \text{ } ^\circ\text{C}$ and vacuum cooled. The solid sample was made from powder taken from the same lot as the powder sample. The steel can and several millimeters of beryllium were machined from the surface of the solid beryllium sample to a final diameter 5 mm and length 20 mm to remove any iron contamination. For consistency in the neutron diffraction measurements, the solid sample was welded into a niobium can similar to the powder.

2.2. Neutron diffraction

Neutron diffraction measurements of the crystallographic thermal expansion were performed on the Spectrometer for Materials Research at Temperature and Stress (SMARTS) at the Lujan Center, LANSCE, Los Alamos National Laboratory. Details of SMARTS are published elsewhere [8], so only a short description is presented here.

SMARTS has a 30-m incident flight path yielding an instrumental resolution of $\Delta d/d = 2.5 \times 10^{-3}$ (full width at half maximum (FWHM)), making it suitable for measuring the small shifts in lattice spacing associated with internal strains. The cylindrical samples were placed vertically in the center of the high temperature vacuum furnace (max. $1800 \text{ } ^\circ\text{C}$) which uses tungsten wire meshes above and below the sample as heating elements. Fig. 1 shows a schematic of the sample and furnace relative to the incident beam and detectors as situated on the SMARTS diffractometer. The beryllium samples in the niobium cans sat on a graphite platform in the center of the hot zone. A thermocouple penetrating the graphite platform and in direct contact with the niobium can was used to monitor the sample temperature in

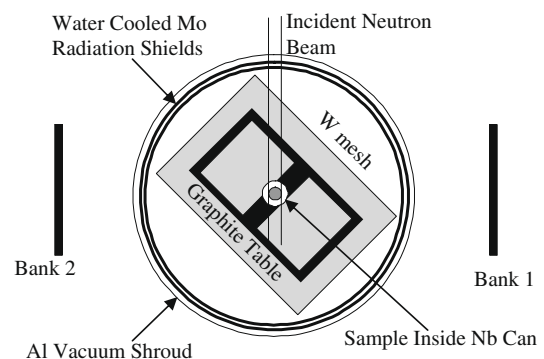


Fig. 1. Schematic (not to scale) of the sample position, furnace and scattering geometry of the SMARTS diffractometer.

real time. However, post-experiment determination of the niobium lattice parameter was used for a more accurate determination of the sample temperature.

Molybdenum radiation shields and water-cooled copper heat shields protect the stainless steel vacuum chamber. Thin, water-cooled aluminum windows in the incident and diffracted beam paths allow passage of the neutrons with minimal attenuation. Strategically placed boron-impregnated shielding prevents parasitic scattering from the vacuum chamber or heat shields from reaching the detector banks on either side of the sample. Each detector bank (referred to from here on as bank 1 and bank 2) consists of 192 ^3He filled tubes and has acceptance angles of $\pm 13^\circ$ in the vertical and horizontal directions. SMARTS has an off-normal view of a water moderator which results in bank 1 having somewhat better peak resolution than bank 2, and most data presented will be from bank 1.

Beryllium is a very good neutron scatterer, and the samples were relatively large. Thus, diffraction patterns of sufficient quality were collected in 4 min for the solid sample and 6 min for the powder (less densely packed). Twenty-minute equilibration times were allowed between temperature changes.

2.3. Data analysis

The diffraction data collected on SMARTS during the heating–cooling cycles was analyzed using the RAWPLOT subroutine contained within the GSAS software. Single peaks were fitted with a Gaussian line shape convoluted with a known instrumental resolution function to find the interplanar spacing of subsets of grains with a common crystallographic orientation (d_{hkl}) relative to the diffraction vector. The diffraction peak FWHM was also determined from the single peak fits and is related qualitatively to the dislocation density. The overall thermal strain was determined by

$$\varepsilon_{hkl}(T) = \frac{d_{hkl}(T) - d_0}{d_0} \quad (1)$$

In this work, d_0 is taken to be the interplanar spacing at 800°C , where the ITR stresses are assumed a priori to be zero. This assumption is borne out by the data.

The calculation of the ITR strains and, subsequently, stresses is worth a brief discussion. The (11.0), and (00.2) represent the principal crystallographic axis of the hcp structure. Owing to the basal plane symmetry, the tensor of thermal expansion adopts the form

$$\alpha = \begin{pmatrix} \alpha_1 & 0 & 0 \\ 0 & \alpha_1 & 0 \\ 0 & 0 & \alpha_3 \end{pmatrix} \quad (2)$$

Similarly, symmetry considerations require that the ITR stress tensor for a grain in a homogeneous isotropic medium, corresponding to the random aggregate, should be diagonal when expressed in crystal axes:

$$\sigma^{\text{ITR}} = \begin{pmatrix} \sigma_{11} & 0 & 0 \\ 0 & \sigma_{22} & 0 \\ 0 & 0 & \sigma_{33} \end{pmatrix}. \quad (3)$$

If only elastic deformation is considered, the stress is also symmetric in the basal plane ($\sigma_{11} = \sigma_{22}$). Further, enforcing the condition of zero macroscopic stresses and averaging the ITR stress tensor over a random distribution of grain orientations leads to the result that $\sigma_{33} = -(\sigma_{11} + \sigma_{22}) = -2\sigma_{11}$. As a consequence, the ITR stress tensor can be written in the simple form

$$\sigma^{\text{ITR}} = \begin{pmatrix} \sigma_{11} & 0 & 0 \\ 0 & \sigma_{11} & 0 \\ 0 & 0 & -2\sigma_{11} \end{pmatrix} \quad (4)$$

Clearly, this assumption for the form of the stress tensor is not valid for any individual grain, but should hold for an average over many grains in the polycrystal, which is what neutron diffraction measures and the EPSC model calculates.

The ITR strains are related to the stresses through the generalized Hooke's law:

$$\varepsilon_{ij} = S_{ijkl} \sigma_{kl} \quad (5)$$

where S_{ijkl} represents the compliance tensor in crystal coordinates. From Eqs. (4) and (5), it is straightforward to show that

$$\varepsilon_{33} = \frac{2(S_{13} - S_{33})}{S_{11} + S_{12} - 2S_{13}} \varepsilon_{11} \quad (6)$$

where the pre-factor in Eq. (6) is -1.9 , given the room temperature single crystal compliance of beryllium [9]. Note that it is assumed that the compliance of beryllium will change little in the relevant temperature range, up to 525°C .

The powder particulates are assumed to be constraint free, and the observed change in interatomic spacing with temperature is solely due to orientation-dependent thermal expansion α_{hkl}

$$d_{hkl}(T) = d_0 + \alpha_{hkl}(T - 800^\circ\text{C})d_0 \quad (7)$$

Recall that d_0 is determined at 800°C , where the ITR stresses are zero. Eq. (7) can be written in terms of lattice strains Eq. (1) as

$$\varepsilon_{hkl}^p(T^p) = \alpha_{hkl}(T^p - 800^\circ\text{C}) \quad (8)$$

Grains in the solid are subject to constraint from their neighborhood (adjacent grains), and the observed strain will be a sum of the thermal expansion and the grain interaction (ITR) strains

$$\varepsilon_{hkl}^s(T^s) = \alpha_{hkl}(T^s - 800^\circ) + \varepsilon_{hkl}^{\text{ITR}}(T^s) \quad (9)$$

The most straightforward way to determine the ITR strains in an arbitrary crystal direction would be to measure the thermal strains in the solid and powder as a function of temperature and simply take the difference

$$\varepsilon_{hkl}^s - \varepsilon_{hkl}^p = \alpha_{hkl}(T^p - T^s) + \varepsilon_{hkl}^{\text{ITR}}(T^s) \quad (10)$$

In practice, if the measurement temperature of both the solid and powder (T^p and T^s) is well controlled and measured, the ITR strains are found trivially by point-by-point subtraction of the strains in the solid and powder samples. In the case of MacEwan et al. [3], the strains measured with diffraction in the solid and a single crystal were fit to polynomials and subtracted.

However, in the case of this experiment the temperature of the beryllium is not known well enough. The temperature of the sample container at each measurement point is determined by the measured lattice parameter and known CTE of the niobium can. Given the CTE of niobium ($7 \times 10^{-6} \text{ }^\circ\text{C}^{-1}$) and the uncertainty in measuring the niobium lattice parameter (20×10^{-6}), the minimum uncertainty is $\pm 3 \text{ }^\circ\text{C}$. Moreover, measuring the temperature of the niobium can is not, in this case, sufficient to determine the temperature of the sample contained in the can. The heat transfer between sample and container is primarily through radiative coupling, which is highly dependent on the surface area of the sample. Because the samples that are being compared are solid and fine powder (i.e., much different surface areas), the transfer of heat between the can and the sample may be different in each case. This is most problematic at relatively low temperatures ($< 300 \text{ }^\circ\text{C}$) as the radiative coupling weakens and, unfortunately, where the ITR strains develop.

Thus, the second term on the right-hand side of Eq. (10) is viewed as the term of interest, and the first term as an uncertainty stemming from the difficulty in knowing the sample temperatures precisely. As Eq. (10) is written, the uncertainty due to the temperature measurement is comparable with the magnitude of the ITR strains. A $5 \text{ }^\circ\text{C}$ temperature difference between the solid and powder sample would result in $\sim 70 \mu\epsilon$ error in the measurement of the ITR strains. Thus, two different (but similar) analysis strategies were chosen to minimize the effects of the temperature uncertainty.

(1) Instead of directly subtracting the lattice strains of solid and powder, the “anisotropy strain” is first calculated:

$$\eta = \epsilon_a - \epsilon_c \quad (11)$$

defined by Daymond et al. [10]. The anisotropy stain is defined in [10] in terms of mechanical as opposed to thermal strains, but the formalism translates well. By analogy with Eq. (10), the ITR strains can be related to the difference of the anisotropy strain measured in the solid and powder by

$$\begin{aligned} \eta^s - \eta^p &= (\alpha_{100} - \alpha_{002})(T^p - T^s) + \epsilon_{10,0}^{\text{ITR}} - \epsilon_{00,2}^{\text{ITR}} \\ &= (\alpha_{100} - \alpha_{002})(T^p - T^s) + 2.9\epsilon_{10,0}^{\text{ITR}} \end{aligned} \quad (12)$$

where the final step stems from Eq. (6) and is dependent on the validity of Eq. (4).

(2) Similarly, instead of direct subtraction of the lattice strains, the c/a ratio of the solid and powder may be subtracted. The derivation is more involved than above, and second-order terms in strain must be discarded, but it can be

shown that the ITR strains can be written in terms of the difference between the c/a ratio of the solid and powder as

$$\begin{aligned} \left(\frac{c}{a}\right)^s - \left(\frac{c}{a}\right)^p &= \frac{[(\alpha_{100} - \alpha_{002})(T^p - T^s) + 2.9\epsilon_{10,0}^{\text{ITR}}]}{1 + (\alpha_{100} - \alpha_{002})(T^p - T^s)} \\ &= \frac{c_0}{a_0} [(\alpha_{100} - \alpha_{002})(T^p - T^s) + 2.9\epsilon_{10,0}^{\text{ITR}}] \end{aligned} \quad (13)$$

where it is recognized that the second term in the denominator is very small compared with 1.

By comparison with Eq. (10), the pre-factor of the “uncertainty” term in Eqs. (12) and (13) decreases by a factor of ~ 5 and, for the second term on the right-hand side, increases by a factor of nearly 3. Thus, the “signal to noise” ratio of the analysis has increased by a factor of 15. Note, however, that the increase in accuracy has come at the cost of an assumption of the form of the ITR strain tensor (Eq. (6) and its derivation), i.e., the calculated strains in the a and c directions of the grains are not independent.

2.4. Model calculations

An upper bound estimate to the ITR stresses and strains can be obtained by assuming a grain with anisotropic CTE, given by Eq. (2), embedded in a matrix with texture-weighted average isotropic CTE. If the differential dilatation between grain and matrix is accommodated elastically by the grain, then

$$\sigma_{ij} = C_{ijkl}(\alpha_{ij} - \bar{\alpha})\Delta T \quad (14)$$

as in Piercy [2] and MacEwan et al. [3]. A more accurate calculation of the ITR stresses comes from similarly placing the grain in a homogeneous isotropic matrix and allowing for elastic equilibration of the inclusion and matrix via Eshelby inclusion theory. The constitutive equations are solved numerically and self-consistently by a computational code, in this case an EPSC code [11]. Specifically, in the case of this work, the polycrystalline aggregate is represented by a set of 23,328 randomly oriented grains, and the properties of the homogeneous matrix are found as the appropriately weighted average over all the grains. It should be noted that the model calculations support the assumptions presented in Section 2.3, specifically Eq. (4).

3. Results

3.1. Sample characterization

Fig. 2a shows the microstructure of the powder as seen by scanning electron microscopy (SEM). The particle size distribution appears bimodal with some very small particulates, i.e., $\sim 5 \mu\text{m}$, and the rest $\sim 35 \mu\text{m}$. Fig. 2b shows optical microscopy from the powder sample, after the neutron diffraction measurements were completed and the powder was infiltrated with epoxy. The low packing fraction of the powder in the can is evidenced by the large portion of epoxy (black). It is apparent that each beryllium particulate is composed of as few as one or as many as

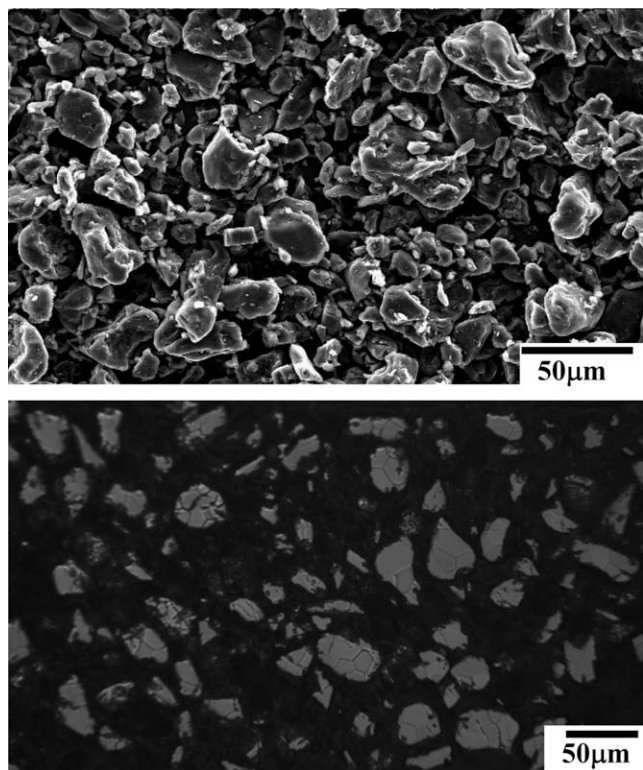


Fig. 2. (a) SEM and (b) optical microscopy of the powder sample.

six grains. This is important, as it was assumed that these grains were free of ITR stresses.

The as-ground powder is expected to be in a heavily worked state, whereas the compacted solid would have effectively annealed during cooling from the compaction temperature of 1000 °C. Thus, during the measurement of the CTE, the powder samples were heated to 800 °C initially, to allow them to anneal, and the thermal expansion was measured on cooling; the solid followed a similar protocol. That annealing was accomplished in the powder is demonstrated in Fig. 3, which shows the FWHM, $\Delta d/d$, of the (11.0) peak of the solid and powder as a function of temperature during heating and cooling. Note that the scatter in the peak width increases markedly at high temperature, because the peak intensity is diminished by the Debye–Waller factor at increased temperature.

The FWHM of the solid is nearly constant at $\sim 0.26\%$ with heating and cooling. In contrast, the FWHM of the powder is initially high at 0.35%, presumably due to the dislocations introduced during grinding. It remains nearly constant up to 200 °C, above which it drops precipitously and levels out at 0.27%, close to the value of the solid at 575 °C. With continued heating and subsequent cooling (during which the CTE measurements were made), the FWHM of the powder peak remains near that of the solid. While the SMARTS diffractometer is not optimized for quantitative determination of dislocation density or twin density from the line profile, it is clear that the powder sample is initially heavily worked, compared with the solid sample, but anneals by 575 °C, and is nearly equivalent

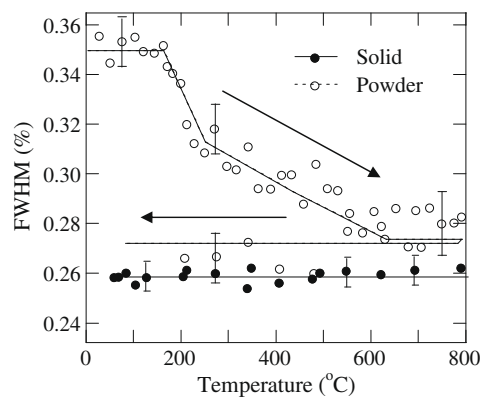


Fig. 3. FWHM ($\Delta d/d$) of the solid and powder samples during heating and subsequent cooling.

to the solid sample microstructurally when the CTE measurements were performed during cooling from 800 °C.

Throughout this paper, the texture of the solid and powder sample will be assumed random. The actual crystallographic textures of the powder and solid sample are represented in the pole figures shown in Fig. 4. The textures were measured using standard time-of-flight (TOF) neutron diffraction techniques on the HIPPO diffractometer [12], while the samples were still encased in the niobium cans. Owing to the approximately spherical shape of the particulate and the lack of packing of the powder, the texture of the powder is nearly random. The solid sample, which was hot pressed, shows a mild texture (max. 1.2 multiples of random distribution) where the basal poles are slightly more likely to be found along a specific direction transverse to the axis of the solid cylinder. Unfortunately, this preferred axis was not tracked throughout the measurement, but model calculation, which will be discussed later, indicates that the weak texture would have a small effect on the ITR stresses, very near or below the level of measurement certainty.

3.2. Thermal expansion results

Fig. 5 shows the development of the lattice strains (referenced to 800 °C) in basal, prismatic and pyramidal lattice planes measured in the solid and powder samples; the

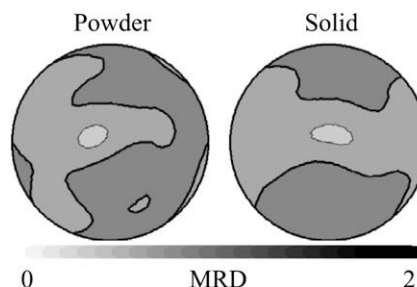


Fig. 4. (00.2) pole figures representing the texture of the solid and powder samples. The bold contour is at 1 multiple of random distribution (MRD) and the contour intervals are at 0.25 MRD. The cylinder axes are off the page.

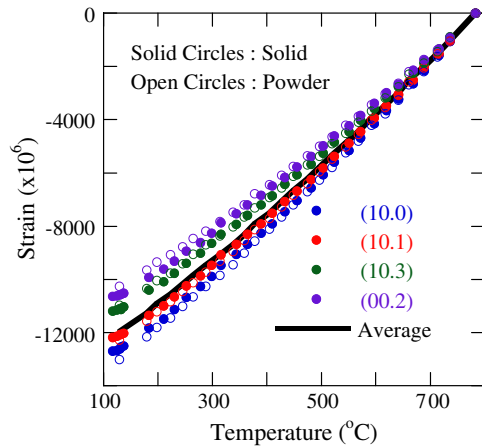


Fig. 5. Lattice strains of several crystallographic orientations in the solid (solid symbols) and powder (open symbols) as a function of temperature. The solid black line represents the texture weighted average lattice strain of the powder.

uncertainties are smaller than the data points. The figure also shows an average crystallographic strain given by $\bar{\epsilon} = \frac{2\epsilon_{100} + \epsilon_{002}}{3}$ [10]. For clarity, only data collected in bank 1 are shown. Further, the diffraction data were of sufficient quality that roughly double the number of independent crystal orientations could have been shown, but only those in the plane of the (10.0) and (00.2) plane normals have been chosen for ease of viewing. As discussed above, the differences between the strains in the solid and the powder are very small compared with the total strain developed during cooling from 800 °C of. In all cases, the strains measured in the solid are closer to the average, owing to the constraining effect on the grains from their neighbors.

3.3. Intergranular thermal residual strains

Figs. 6 and 7 show the development of the anisotropy strain ($\eta = \epsilon_{100} - \epsilon_{002}$) and the c/a ratio, respectively, as a function of temperature during cooling. Results from both

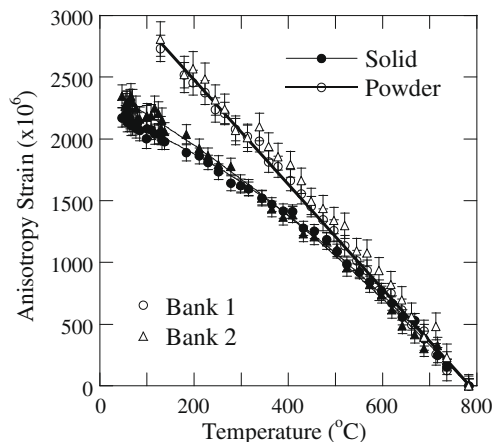


Fig. 6. Anisotropy ($\epsilon_{10.0} - \epsilon_{00.2}$) strain in the solid (solid symbols) and powder (open symbols) developed during cooling. Data collected in bank 1 are represented by circles, bank 2 by triangles.

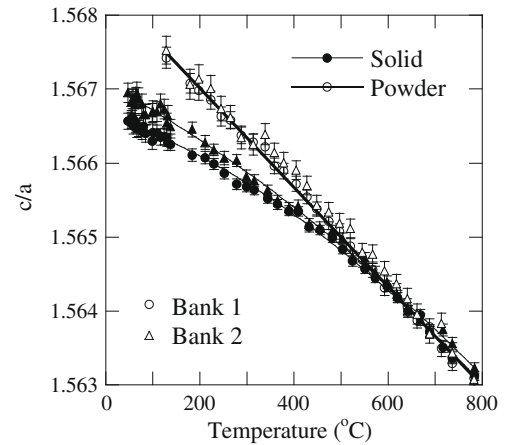


Fig. 7. c/a ratio in the solid (solid symbols) and powder (open symbols) developed during cooling. Data collected in bank 1 is represented by circles, bank 2 by triangles.

bank 1 and bank 2 are included. The uncertainties are derived solely from the statistical uncertainties associated with the peak fitting. In the powder, both the anisotropy strains and the c/a ratios determined from data collected in bank 1 and 2 are within uncertainty of each other and are linear with temperature. Also, above 575 °C, both parameters determined in the solid are equivalent to that determined in the powder, to within the measurement uncertainty. Below 525 °C, the anisotropy strain and c/a ratio of the solid deviate from linearity (and from the powder behavior) as the ITR stresses begin to develop.

It is worth noting that the anisotropy strain and c/a ratio determined from data collected in banks 1 and 2 deviate slightly from each other <575 °C; the deviation is near the level of uncertainty. The EPSC model calculations of the ITR strains (to be discussed in detail later) show that the difference between the results in banks 1 and 2 is consistent with the presence of a weak texture in the solid sample if the sample were oriented in a certain orientation. As the difference is near the limit of measurement uncertainty, and the orientation of the solid was not tracked throughout the measurement, the difference will be ignored, and the results from banks 1 and 2 will be averaged.

4. Discussion

The ITR stresses derived from the measured lattice strains and temperature-independent elastic constants [9] are shown in Fig. 8; the uncertainties have been propagated from the statistical uncertainties of the peak fitting. The ITR stresses are not significantly different from zero at $> \sim 575$ °C, indicating that the stresses that should develop due to the CTE anisotropy are relaxed on the timescale of the neutron diffraction measurements. This point is referred to as the “zero strength temperature”. Interestingly, this corresponds well to the temperature at which the heavily worked powder was completely annealed on heating, as judged by the evolution of the peak width shown in Fig. 3.

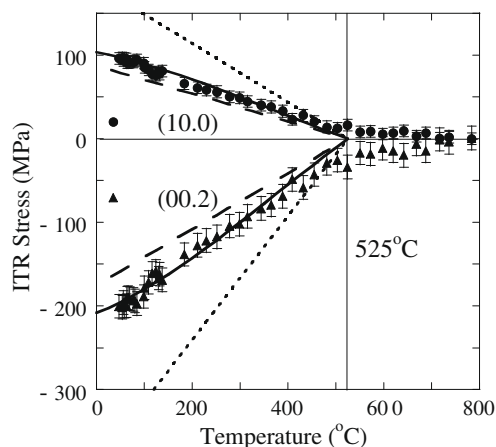


Fig. 8. Intergranular thermal residual stresses developed in solid beryllium during cooling from 800 °C. The dotted line represents an upper bound calculation of the stresses, the dashed line an Eshelby calculation assuming the room temperature crystallographic CTE, and the solid line an Eshelby calculation using the temperature-dependent CTE.

Below 525 °C, and down to room temperature, the ITR stresses and strains increase nearly linearly. Along the *c* axis, the stresses at room temperature are compressive and ~ -200 MPa; the *a* axis stresses are 100 MPa. The yield strength of powder processed beryllium at room temperature is typically cited near 300 MPa. Thus, the ITR stresses are a significant fraction of the yield point and would certainly affect the micro-mechanics of deformation, that is, which grain orientations yield first under a given loading direction and on which deformation system, as suggested in Ref. [7]. Between 575 °C and 525 °C, the ITR stresses increase to just above the limit of uncertainty, but are not yet on the nearly linear trend to room temperature.

The development of the ITR stresses <525 °C has been calculated by models of varying complexity, and the results are shown in Fig. 8. The simplest is to assume each grain resides in a neighborhood with the texture weighted average thermal expansion of the material and an infinite stiffness, as was done by Piercy [2] and MacEwan et al. [3]. This simple model is recognized to be an upper bound to the ITR stresses. The result of this calculation is represented in Fig. 8 by a dotted line and overpredicts the ITR stresses by a factor of ~ 2 , similar to the result of MacEwan et al. [3]. More complicated but much more accurate is an EPSC model calculation similar to that used by Tomé et al. [4] and Pang et al. [5] and discussed above. The dashed line in Fig. 8 represents the results of the EPSC model with the crystallographic CTE held constant at their room temperature values. In this case, the model underpredicts the ITR stresses by $\sim 20\%$. Finally, an EPSC calculation was also performed with temperature-dependent CTE taken from the literature [6] (which are consistent with those measured in this work), and the results are represented by a solid line in Fig. 8. The data are well reproduced by the model calculation <525 °C when using the temperature-dependent CTE and not allowing for plastic relaxation during cooling.

Between 525 °C and 575 °C, there is a region of curvature of the measured ITR stresses, where the stresses are slightly larger than the uncertainty, but not yet following the linear dependence to room temperature. This could be interpreted as a region in which the ITR stress increase is controlled by the (low) yield strength of the plastic systems. Temperature-dependent yield strength could have been included in the EPSC model to reproduce this region of curvature, but the stresses are so close to uncertainties that the efforts were not deemed warranted.

Thus, the development of the ITR stresses measured using neutron diffraction may be broken into three regions: (1) >575 °C the material flows freely to relax the ITR stresses; (2) <525 °C the ITR stresses increase elastically without reaching the increasing yield strength; and (3) a small transition region between 525 °C and 575 °C, where plasticity limits the growth of the ITR stresses.

5. Conclusions

Direct measurements of the ITR strains developed in solid beryllium during cooling from 800 °C and model calculations of the strains are reported. The measurements were completed by comparison of crystallographic parameters measured in a solid and a powder sample as a function of temperature. Above 575 °C, the solid beryllium lacks the strength to maintain these short-length-scale stresses over the timescale of the measurements, and they are observed to be zero within uncertainty. Between 575 °C and 525 °C, the ITR stresses begin to increase, but are limited by the flow strength of the material. Below 525 °C, they increase nearly linearly with room temperature, but do not exceed the flow strength. At room temperature, the *c* axis of an average grain in the polycrystalline solid sample sustains ~ -200 MPa of stress, which is to be compared with the yield point of ~ 300 MPa for powder-compacted beryllium. Eshelby-type model calculations reproduce well the observed data <525 °C if the temperature-dependent CTE are used, and no plasticity is allowed in the model.

These short-length-scale stresses undoubtedly play a role in the micro-mechanics of deformation (i.e., which grain orientations yield first and on which system). They are ubiquitous in lower symmetry (non-cubic) materials with anisotropic crystallographic thermal expansion coefficients and cannot be annealed by any heating technique because subsequent cooling to room temperature will inevitably reform them.

Acknowledgements

This work has benefited from the use of the Lujan Neutron Scattering Center at LANSCE, which is funded by the Office of Basic Energy Sciences (DOE). Los Alamos National Laboratory is operated by Los Alamos National Security LLC under DOE Contract DE-AC52-06NA25396. C.N.T. acknowledges financial support from

Office of Basic Energy Science (DOE) through Project FWP 06SCPE401.

References

- [1] Somasundaram R, Premanand V. *J Nucl Mater* 1966;19:283.
- [2] Piercy GR. *J Nucl Mater* 1968;26:18.
- [3] MacEwen SR, Tomé C, Faber J. *Acta Metall* 1989;37:979.
- [4] Tomé CNC, Turner N, Miller P, Woo M, Root CH, Holden TM. *J Nucl Mater* 1996;227:237–50.
- [5] Pang JW, Holden TM, Turner PA, Mason TE. *Acta Mat* 1999;47:373.
- [6] Touloukian YS, Kirby RK, Taylor RE, et al. *Thermal expansion: metallic elements and alloys*. New York: Plenum; 1975.
- [7] Brown DW, Bourke MAM, Clausen B, et al. *Met Trans A* 2003;34:1439.
- [8] Bourke M, Dunand D, Ustundag E. *Appl Phys A* 2002;74:S1707.
- [9] Simmons G, Wang H. *Single crystal elastic constants and calculated aggregate properties*. Cambridge (MA): Massachusetts Institute of Technology; 1971.
- [10] Daymond MR, Bourke MAM, VonDreele RB. *J Appl Phys* 1999;85:739.
- [11] Turner PA, Tomé CN. *Acta Met* 1994;42:4143.
- [12] Wenk H, Lutterotti L, Vogel S. *Nucl Instrum Methods Phys Res A* 2003;515:575.